19th Brazilian Congress of Thermal Sciences and Engineering
November 6th–10th, 2022, Bento Gonçalves - RS - Brazil

ENC-2022-0726
Analysis of a compact cooling system containing an enhanced-surface spray heat sink

Marcus Vinícius Pedron Carneiro[1] **André Provensi**[2]
Pedro Cavicchioli[1]
Milton Pereira[3]
Jader Riso Barbosa Jr.[1,*]
[1] POLO - Research Laboratories for Emerging Technologies in Cooling and Thermophysics, Department of Mechanical Engineering, Federal University of Santa Catarina, Florianópolis, SC, Brazil
[2] Akaer Engenharia S.A., Technological park, São José dos Campos, São Paulo, SP, Brazil
[3] LMP - Precision Engineering Laboratory, Department of Mechanical Engineering, Federal University of Santa Catarina, Florianópolis, SC, Brazil
carneiro@polo.ufsc.br
andreprovensi@gmail.com
cavicchioli.pedro97@gmail.com
milton.pereira@ufsc.br
jrb@polo.ufsc.br*

Abstract. *In previous studies, we introduced the concept of a compact heat sink that combines an evaporator and an expansion device into a single unit for high heat flux applications. As the high-pressure subcooled liquid refrigerant expands in an array of oblique orifices, a spray cone is formed which directly impinges on the heated surface, removing large quantities of heat by boiling and evaporation of the liquid film. Numerous applications of the concept can be sought when one considers its integration with compact compressors (i.e., cooling of power electronics, batteries etc.), since it combines the low thermal resistance of impinging jets with below-ambient evaporating temperatures. In this paper, we evaluate the use of laser-ablated square micro pillars on the heated surface as a means to enhance the heat removal capability of the system. Microscopic and interferometry images of the resulting surfaces are presented and evaluated regarding its final topography and extended heat transfer surface area. Experiments conducted with R-134a using a two-orifice expansion device and enhanced surfaces resulted in a cooling capacity of 230 W (35.9 W/cm^2) with a heated surface temperature always below 22.9 °C and average heat transfer coefficients as high as 46,369 W/(m^{2}K). In comparison with mirror polished surfaces, this represents a thermal conductance increase of 91%, resulting in a significant reduction of the heated surface temperature.*

Keywords: *electronics cooling, spray cooling, refrigeration system, enhanced surfaces*

1. INTRODUCTION

The demand for high-power electronic chips, supercomputing, hybrid vehicles and other technological products with increasing performance requirements has set thermal management of electronics as a centerpiece of the technology development (Lijun *et al.*, 2020; Li *et al.*, 2020; Shurong *et al.*, 2020; Rong *et al.*, 2021). In recent years, substantial efforts have been made towards developing novel cooling solutions for high heat fluxes since traditional single phase cooling technologies are no longer able to meet the stable and reliable cooling requirements. Under these circumstances, phase-change cooling must be applied to keep the components temperature below the limit one at these severe conditions (Wiedenheft *et al.*, 2017; Khandekar *et al.*, 2021).

In this context, Oliveira and Barbosa Jr. (2017a) presented a miniaturized active cooling solution based on the direct impingement of single and multiple sub-cooled liquid jets on a circular heated element. This solution combines the low thermal resistance of impinging jets with the below-ambient evaporating temperatures of vapor compression systems. Later, Carneiro *et al.* (2018) and Carneiro and Barbosa Jr. (2021) evaluated different jet and spray atomization strategies in the refrigeration system of Oliveira and Barbosa Jr. (2017a). The analysis presented are based on the cooling system thermodynamic performance and steady-state heat transfer parameters. High-speed video sequences were used to

elucidate the heat transfer features.

Jet impingement and spray cooling are recognized as promising solutions to sustain high heat transfer coefficients at high heat fluxes. The liquid droplets from these cooling schemes create a thin liquid film on the top of the heated element, removing a large quantity of heat by boiling and evaporation (Parizad Benam *et al.*, 2021). The refrigerant droplets impinging frequency and momentum promote high frequency bubble grow and breakup, contribute to increase convection and allow the droplets to penetrate the vapor film at the film boiling regime (Carneiro *et al.*, 2018; Carneiro and Barbosa Jr., 2021). These heat transfer features contribute to bring forward the onset of nucleate boiling and increase the critical heat flux (CHF) (Yang *et al.*, 1996).

The CHF is characterized by a sudden increase of the heater temperature, which has been observed to be unleashed by partial or total dryout of the liquid film on the heated surface (Carneiro *et al.*, 2018). Carneiro and Barbosa Jr. (2021) also observed that the dryout process started from the outer region of the circular heater and gradually moved towards the center as the heat load was increased. Therefore, in order to sustain higher heat fluxes, a possible alternative is to include the use of enhanced surfaces to increase the residence time and distribution of the liquid on the heated surface (Carneiro *et al.*, 2020; Xu *et al.*, 2021).

Micro- and nano-engineering allows the manufacturing of complex topographies, however, the mechanisms of spray cooling enhancement by surface engineering are very diverse and ambiguous (Silk *et al.*, 2006). In this paper, we evaluate laser-ablated surfaces with simple square micro pillars of different sides and spacing. Microscopic and interferometry images are used to assess the resulting surface, measure the extended heat transfer surface area and evaluate its influence on the refrigeration system thermodynamic performance and heat transfer parameters.

2. EXPERIMENTAL WORK

2.1 Experimental apparatus

The main features of the mechanical vapor compression refrigeration loop are highlighted in Figure 1 while its detailed description has been presented elsewhere (Oliveira and Barbosa Jr., 2017a,b). The proposed cooling principle is based on the liquid-vapor phase change of two-phase jets that expand as they flow through orifices and impinge on a heated surface. Therefore, this approach allows to integrate the function of the expansion device and evaporator of a conventional vapor compression refrigeration system into a single unit. The refrigeration system is a R-134a loop driven by a compact, high-frequency, oil-free, linear-motor compressor (1). The condenser (3) is a compact brazed plate counter-flow heat exchanger, which rejects heat to an ethylene glycol solution loop. The cooling unit (4) is positioned downstream of the condenser. A compressor suction line heater (5) guarantees that no liquid enters the compressor, by maintaining a fixed inlet superheat. The calorimeter (10) houses the compressor and uses an air heater (8) and a thermoelectric (Peltier effect) cooler (9) for fine temperature control.

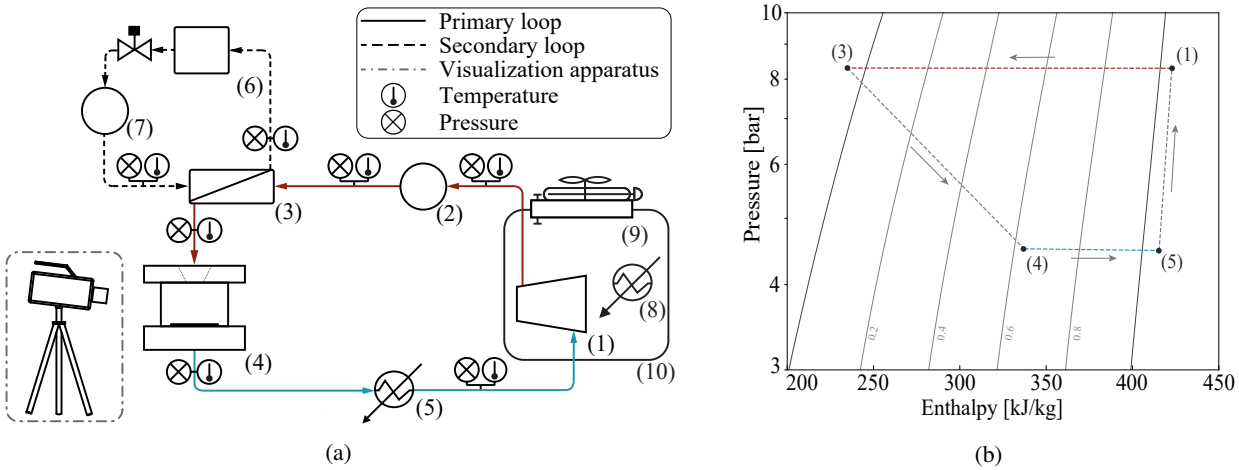

(a) (b)

Figure 1: (a) Schematic diagram of the experimental apparatus. (b) *p-h* diagram of the thermodynamic cycle. Adapted from Carneiro and Barbosa Jr. (2021).

The refrigerant and the ethylene glycol solution flow rates are measured by Coriolis effect (2) and paddle wheel flow meters (7), respectively. Pressure and temperature are measured at several points along the primary and secondary loops. Figure 1(b) presents the *p-h* diagram of the thermodynamic cycle for a generic operating condition. The thermodynamic points are the ones at the outlet of their respective components presented in Figure 1(a).

Table 1 lists the measuring devices used in the experimental apparatus with its expanded and relative uncertainties.

Measured quantity	Instrumentation	Expanded uncertainty
R-134a mass flow rate	Coriolis effect flow meter	0.05 kg/h (0.17%)
Cooling mixture volumetric flow rate	Paddle wheel flow meter	0.07 L/min (1.47%)
Absolute pressure (hot side: 0 – 30 bar)	Strain-gage pressure transducer	0.05 bar (0.16%)
Absolute pressure (cold side: 0 – 10 bar)	Strain-gage pressure transducer	0.03 bar (0.3%)
Power consumption	Digital power meter	0.3 W (0.02%)
Calorimeter and room temperatures	Type T thermocouple	0.22 °C
Temperature	PT-100	0.20 °C

Table 1: Measured quantities and instrumentation used in the experimental work.

2.2 Cooling unit

The cooling unit is a sealed chamber that houses the heat transfer surface. Its exploded CAD view is presented in Figure 2(a) along with the main components. Sub-cooled liquid from the condenser enters the spray cooling unit through a metallic cap that confers mechanics integrity. The refrigerant flows through the orifice section, Figure 2(b), containing two oblique equally spaced orifices with 12.035 mm in length and 500 μm in diameter. The orifices produce free jets that converge at a single collision point inside the visualization chamber of the cooling unit, further detailed in Carneiro *et al.* (2018). Downstream of the collision point, the jets break up into a spray, which impinges on the heat transfer surface, Figure 2(c).

The surface of interest, also addressed as impinging surface, is the top surface of a cylindrical copper block with a surface area A_s = 6.4 cm^2. The copper block seats on the top of a NiCr film heater. The heating elements (film heater and copper block) are positioned in the so-called insulation and drainage unit, Figure 2(a). This unit thermally insulates the side and bottom of the heating components and allows the vapor and remaining liquid to exit the cooling unit through the bottom.

The NiCr film heater generates the system thermal load from a DC power supply. However, a fraction of the Joule heating power may be dissipated at surfaces other than the impinging surface. Therefore, a wide range of thermal conductance at the two-phase target surface were simulated and numerically evaluated to be smaller than 5% (Oliveira and Barbosa Jr., 2017b).

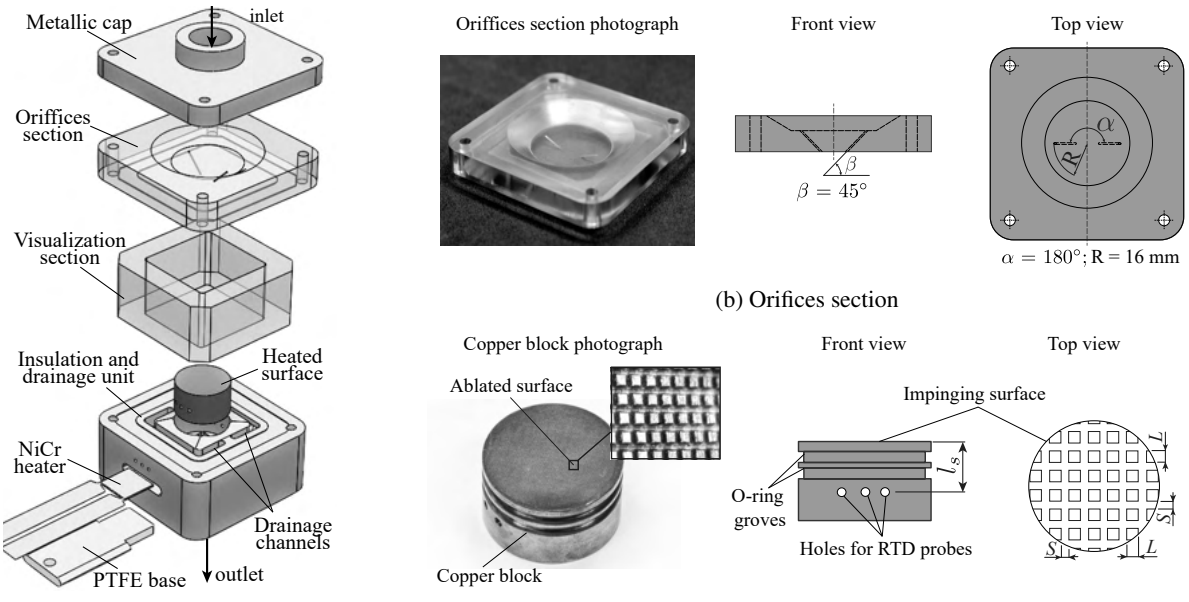

(a) Exploded view of the cooling unit

(b) Orifices section

(c) Schematic representation of the heated surface

Figure 2: Cooling unit main components and geometry. Adapted from Carneiro *et al.* (2020).

2.3 Impinging surface

Figure 2(c) shows the geometry of the copper block. It contains six holes where resistance temperature detectors (RTDs) are positioned to measure the block temperature in a horizontal plane below the surface of interest. The impinging surface temperature is determined by an extrapolation of Fourier's Law using the average temperature of the six RTDs, $\overline{T}_{RTD}$, the fraction of the total input power that reaches the surface of interest (95% of the skin heater power heat load)

and the distance between the surface of interest and the plane containing the RTDs, l_s = 10.03 mm.

Squared micro pillars were fabricated on the impinging surface using a nanosecond pulsed fiber laser IPG YLPN-1-1x120-50-M. To focus and scan the laser beam, a two-mirror galvanometric scanner Aerotech AGV-14HPO with a 170 mm lens is used (Martendal *et al.*, 2020). Prior to the ablation process, all ablated surfaces were sanded using a 400-mesh sandpaper. This grit size results in lower contact angles for copper alloys (Kubiak *et al.*, 2011). To produce the micro pillars, the laser first ablates the surface in one direction all over the copper block. Then, the process is repeated in the perpendicular direction. The squared micro pillar manufacturing parameters are the laser beam 2000 mm/s velocity, 150 Hz frequency, 50 ns pulse width, 50 W in power and the laser wavelength of 1064 nm.

The surface geometry resulting from the ablation process is shown in Figure 2(c), where L and S are the size and spacing of the square micro pillars (nominal dimensions). In total, 11 surfaces are evaluated in this work, two of which are not ablated. The first one is the smooth surface with a mirror polished finishing and the second is the baseline surface with 400-mesh sandpaper finishing. The 9 ablated surfaces are named accordingly to their geometry as "S***" and "L***", where "***" represents the micrometers of the dimensions presented in Figure 2. Thus, the S200 L400 surface, for example, presents a space between pillars, S, of 200 μm and a squared pillar side, L, of 400 μm.

The resulting surface topography was evaluated with a microscope (LEICA DM 4000M) and an interferometer (Zygo NEWVIEW 7300). Figures 3(a) and (b) illustrates the microscopic and interferometry images for the S200 L400 surface, respectively. The microscopic image shows the top view of the heated surface indicating a good regularity and alignment of the micro pillars. The microscopy indicates the presence of straight dark lines along the board of each pillar and also connecting one another. The reason for these dark regions become clear once the interferometry images are analyzed. Figure 3(b) indicates that the pillar walls are not perfectly vertical and points to the existence of cavities in the junctions between pillars. While the inclined walls are a result of the fixed laser focus point, the cavities are a consequence of laser beam trajectory since it removes material twice in the junctions (once when moving horizontally and a second time when moving in the perpendicular direction).

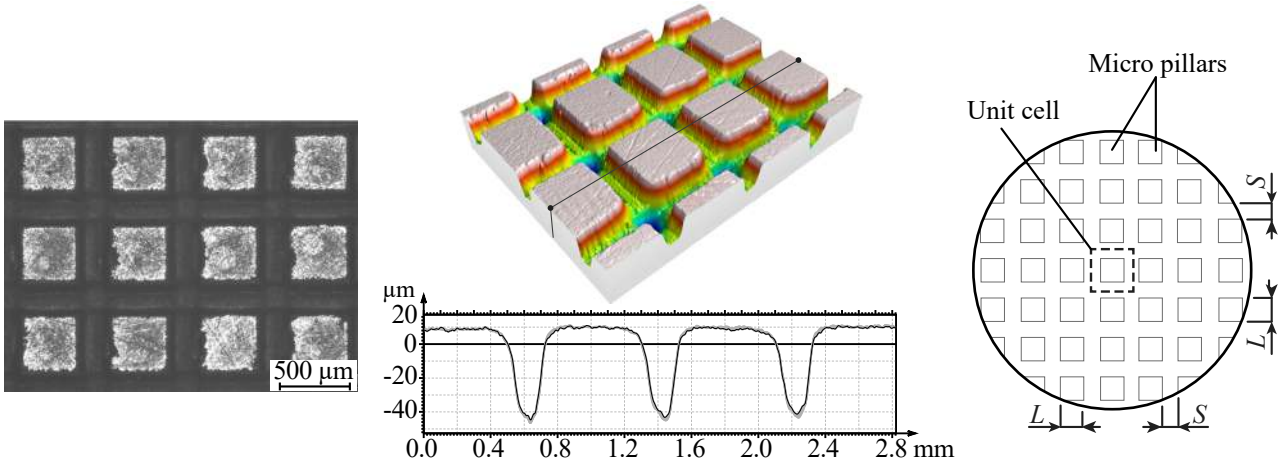

(a) Microscopy (b) Interferometry (c) Unit cell representation

Figure 3: Cooling unit main components and geometry. Adapted from Carneiro *et al.* (2020).

The microscopy results also indicate small scratches on the top surface and few irregularities on the edge of some micro pillars. As these features are compared to the inteferometry results, a good agreement among both surface imaging is observed once more. The surface scratches are a result of the sanding process prior to the ablation process and indicate that the ablation only slightly affected the original surface. On the other hand, the few irregularities on the edge of the pillars may be related to desublimation of the ablated material.

Finally, the interferomety may indicate quantitatively the dimensions of each feature observed in the resulting surface. Therefore, the total surface area of the new impinging surface can be determined by means software analysis. The evaluation of this quantity allows to the correction of the heat transfer surface area in order to eliminate the effect of the surface extension on the heat transfer coefficient. To that end, a unit cell is defined as presented in Figure 3(c). The extended surface is calculated as

$$A_s^* = A_s \frac{A_t}{A_p} \tag{1}$$

where A_t/A_p is the total to the projected surface area ratio in a unit cell.

Due to the COVID-19 pandemic, no interferometry image was obtained for the S200 L200 surface. Thus, its total to

projected surface area ratio was obtained by means of a curve fitting based on the measured S and L dimensions,

$$\frac{A_t}{A_s}(S, L) = b_0 + b_1 S + b_2 L \tag{2}$$

with b_0, b_1 and b_2 are 1.2043, 1.3997e-4 and -1.447e-4, respectively.

Table 2 summarizes the measurements conducted with MountainsLab software for the ablated surfaces.

Surface	S	L	A_t	A_p	A_s/A_p	A_s^*
S200 L200	200	200	–	–	1.147†	7.343†
S200 L400	255.2	349.7	426.421	382.473	1.115	7.135
S200 L600	262.4	537	724.828	664.351	1.091	6.982
S400 L200	456.1	155.4	410.24	363.545	1.124	7.222
S400 L400	459	341.6	791.462	730.673	1.083	6.932
S400 L600	463.8	535.7	1.055.93	996.898	1.059	6.778
S600 L200	668.7	145.3	696.907	643.945	1.082	6.926
S600 L400	682.2	340.8	1133	1064	1.065	6.815
S600 L600	641.4	556.5	1580	1487	1.062	6.8

Table 2: Values for the ablated surfaces geometry († calculated).

2.4 Experimental conditions and procedure

Experiments were conducted to investigate the influence of the applied thermal load and surface enhancement on the system and cooling unit thermal performance. The compressor was operated at its maximum volumetric displacement. The hot sink temperature and the refrigerant superheat at the compressor were kept fixed at 25°C and 10°C, respectively. A orifices section with two oblique (colliding) jets and a visualization section height (distance between the orifices and the target surface) of 23.8 mm were used.

Tests are conducted in the heat-up mode, increasing the thermal load gradually (in steps of 25 W) until an unstable temperature reading, associated with the CHF, is reached. As a safety precaution, a cut-off temperature was set to 68°C. Once this temperature is reached, the last stable point along the boiling curve is repeated and a new 5-W step is taken until the next temperature runaway. After the second temperature runaway, the test is ended and the last recorded heat flux point is considered the CHF.

In order to provide a meaningful basis for comparing the results for different surfaces, a baseline refrigerant mass flow rate (0.83 g/s) is enforced in the test at the lowest thermal load (25 W). Thus, the refrigerant charge is adjusted for every new surface setup and kept constant during the entire heat-up test.

Every experimental run was checked for consistency with respect to the overall energy balance in the experimental setup. The expanded uncertainties were calculated and are presented together with the experimental data for each experimental point.

Prior to each experimental test, the assessed surface is immersed in a H_2SO_4 solution (10% vol.) for 10 minutes to remove the copper oxide residue from the ablation process. Next, the surface is immersed in deionized water for 5 minutes to remove any H_2SO_4 excess. Finally, the excess water is blown with compressed dry air.

2.5 Data regression

The specific enthalpy state at the outlet of the spray cooling unit, $h_{jc,o}$ was calculated by means of an energy balance, neglecting thermal losses and the kinetic and potential energy contributions. Since the refrigerant enters the cooling unit as subcooled liquid, the inlet specific enthalpy, $h_{jc,i}$, is computed using the measured pressure and temperature at the inlet point (Bell *et al.*, 2014). Therefore,

$$h_{jc,o} = h_{jc,i} + \frac{\dot{Q}_c}{\dot{m}_r} \tag{3}$$

where $\dot{m}_r$ is the refrigerant mass flow rate and $\dot{Q}_c$ is the film heater thermal load.

The evaporating and condensing pressures, respectively p_{evap} and p_{cond}, were assumed equal to the pressures at the outlets of the cooling unit and condenser, respectively. Thus, the evaporating and condensing temperatures, respectively T_{evap} and T_{cond}, are the saturation temperatures at p_{evap} and p_{cond}, respectively.

The vapor mass quality at the outlet of the cooling unit, $x_{jc,o}$ is computed as a function of $h_{jc,o}$ and the pressure measured at this point, which is the evaporating pressure.

The heated surface temperature, T_s, was determined through a linear extrapolation of the Fourier's law considering 1-D heat conduction in the axial direction,

$$T_s = \overline{T}_{RTD} - \frac{l_s \dot{Q}_c^*}{k_s A_s} \tag{4}$$

where k_s is the thermal conductivity of copper at $\overline{T}_{RTD}$ and $\dot{Q}_c^*$ is the fraction of the thermal load reaching the heater surface (95% of $\dot{Q}_c$). The jet impingement heat transfer coefficient, $\hbar_s$, is calculated as

$$\hbar_s = \frac{\dot{Q}_c^*}{A_s(T_s - T_{evap})} \tag{5}$$

The coefficient of performance, COP, is defined as

$$COP = \frac{\dot{Q}_c}{\dot{W}_{comp} + \dot{W}_{fan}} \tag{6}$$

where $\dot{W}_{comp}$, is the measured electrical power consumption of the compressor and $\dot{W}_{fan}$ is the power required to drive the fans inside the calorimeter.

Finally, as an attempt to separate the extended heat transfer surface area effect from the other heat transfer enhancement mechanisms due to the surface enhancement, such as number of nucleation sites, capillary driven force and wetting effects, a corrected heat transfer coefficient can be defined as

$$\hbar_s^* = \frac{A_s}{A_s^*} \hbar_s \tag{7}$$

3. Results

Figure 4 presents the refrigerant mass flow rate for all the evaluated surfaces. At the heat load of 25 W, it can be observed the common starting point for all the curves, ranging within the measured uncertainty. The refrigerant mass flow rate increases systematically with the heat load. These first results show that the enhanced surface setup result in different number of experimental points. This is due to the different CHF reached with each assessed surface. In addition, despite the small discrepancy for the last experimental point of the smooth surface, the refrigerant mass flow rate at each experimental point is virtually the same for all surfaces.

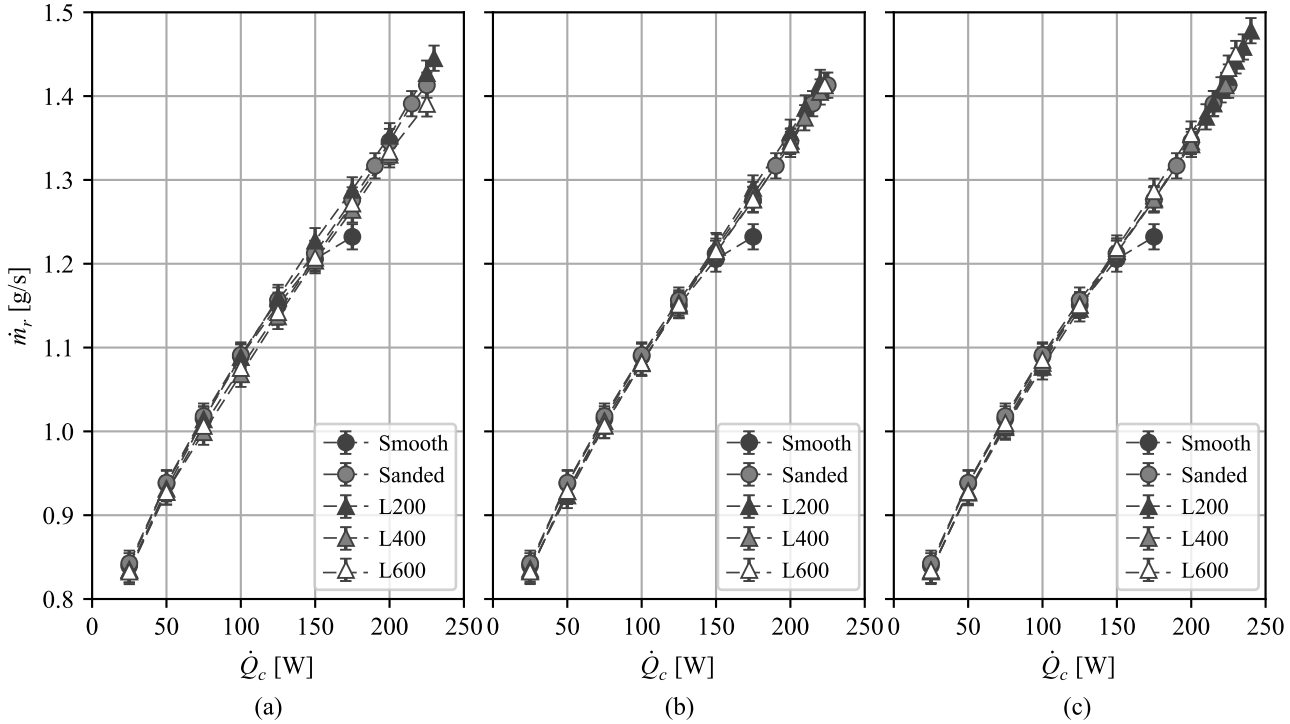

Figure 4: Refrigerant mass flow rate. Micro pillars spacing (a) S200, (b) S400, (c) S600.

Figure 5 presents the saturation temperatures and it indicates that the evaporating and condensing temperatures follow the same trend for all surfaces. The evaporating temperature rises more significantly than the condensing temperature as

the applied heat load is increased. Thus, this results in increasing evaporation pressures and, consecutively, larger densities and refrigerant mass flow rate. Furthermore, as in the refrigerant mass flow rate results, the evaporating temperature is not greatly affected by the heat transfer geometry, what indicates that the refrigeration system operates at similar thermodynamic states despite the surface geometry and finishing.

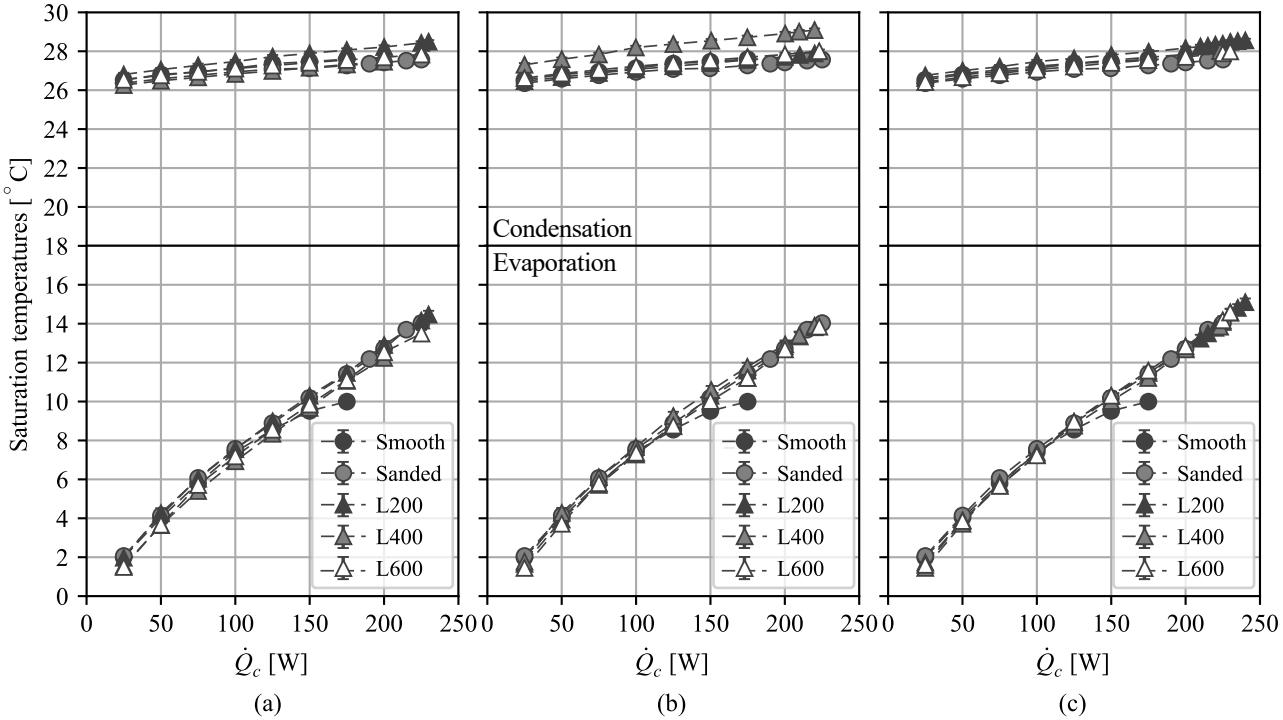

Figure 5: Saturation temperatures. Micro pillars spacing (a) S200, (b) S400, (c) S600.

The compressor electrical power consumption is presented in Figure 6. As expected, the similar evaporation pressures for all the evaluated surfaces, fixed superheating degree and constant piston stroke, the volumetric efficiency may be equivalent for all experimental curves. Therefore, the power consumption is essentially the same. For simplicity, only one uncertainty bar is presented to indicate that all experimental results are within it.

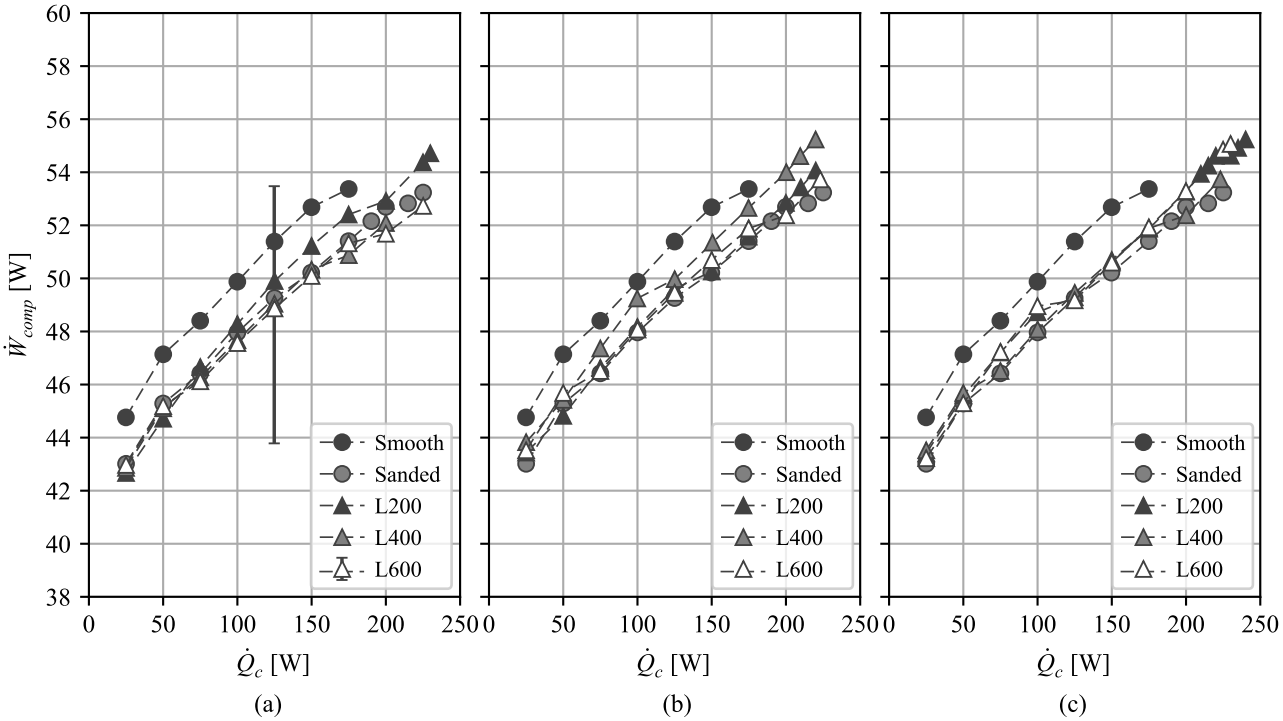

Figure 6: Compressor electrical power consumption. Micro pillars spacing (a) S200, (b) S400, (c) S600.

The compressor electrical power consumption result is consistent with the one presented for the saturation temperatures, Figure 5, since the evaporating temperature increases more significantly than the condensing temperature with the increasing heat load. This increasing pressure is responsible for a larger density, what increases the refrigerant mass flow rate.

Another important point to consider is that all the curves presented virtually the same results for the mass flow rate and saturation temperatures. This result and the knowledge that a fixed superheating degree is given, ensures that a similar thermodynamic state is observed for all the heating surfaces at the inlet of the compressor. It is also important to acknowledge that a similar inlet condition may result in a similar volumetric efficiency, that is why the electrical power consumption is virtually the same for all the experimental setups. Figure 6 presents these results. Since the electrical power consumption presents a relative large measuring uncertainty, only the uncertainty bar for the L600 surfaces are presented with all the results for the other surfaces lying within.

Figure 7 presents the system coefficient of performance as a function of the applied heat load. Similarly to the compressor electrical power consumption result, the COP for all tested surfaces presented the same trend and a performance within the measuring uncertainty. These results indicate the refrigeration system integrity and stability since the surface enhancement does not influence the thermodynamic performance. That result may be a consequence of how the cooling unit is designed. The heat load in this solution is the input parameter and the heat transfer coefficient is independent of the heat transfer rate. Therefore, surface temperature is the dependent variable instead of the heat load.

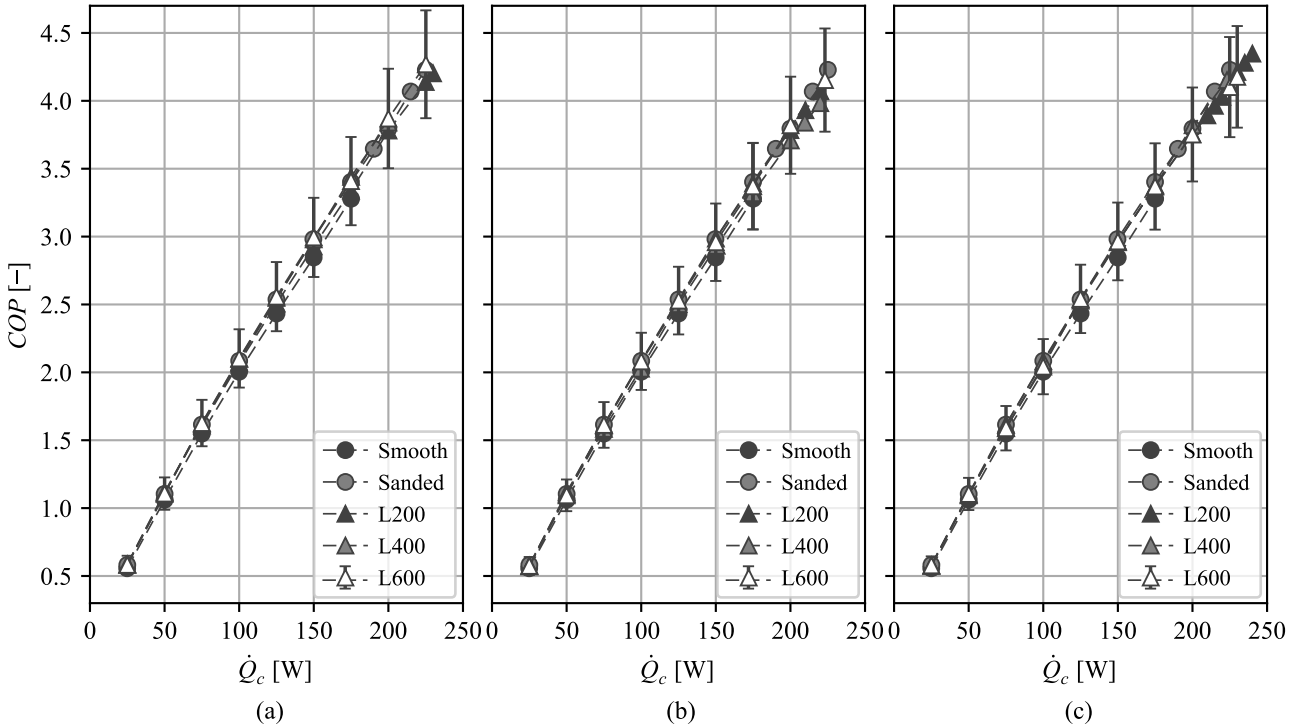

Figure 7: Coefficient of performance. Micro pillars spacing (a) S200, (b) S400, (c) S600.

Figure 8 present the heated surfaces temperatures as a function of the applied heat load. In general, it is noticed that all surfaces presented a reduction in the increasing temperature rate for heat load values between 75 - 175 W. That is an evidence of the thermal conductance enhancement as the heat load is increased. Furthermore, as the heat load approaches the CHF value, all surface temperatures increases sharply, converging between 26 - 35°C.

For the surface temperature standing point of view, the sanded surface is the less effective among the modified one. This surface presented temperatures below the smooth one for heat loads above 50 W with a more significant temperature reduction at heat loads above 150 W. On the other hand, the ablated surfaces presented temperature below that of the sanded and smooth surfaces for all heat transfer rates.

Once the S and L are considered in the heat transfer surface temperate analysis, it is clear a inverse proportionality between the pillars spacing and the surface temperature reduction performance. For example, the larger spacing, S600, presented temperature values closer to the sanded surface. In addition, as the space between pillar decreases, more detached the surface temperature curves are from the sanded and smooth ones. A possible explanation to this behavior may lie on the capillarity effect, which enhances as the space between pillars reduces. The larger capillary pumping contributes to a better liquid distribution over the heated surface and the liquid supply near the edge of the surface. Nonetheless, to better understand the capillary effect, other effects may be subtracted, such as the heat transfer surface area extension, which will be addressed in this paper.

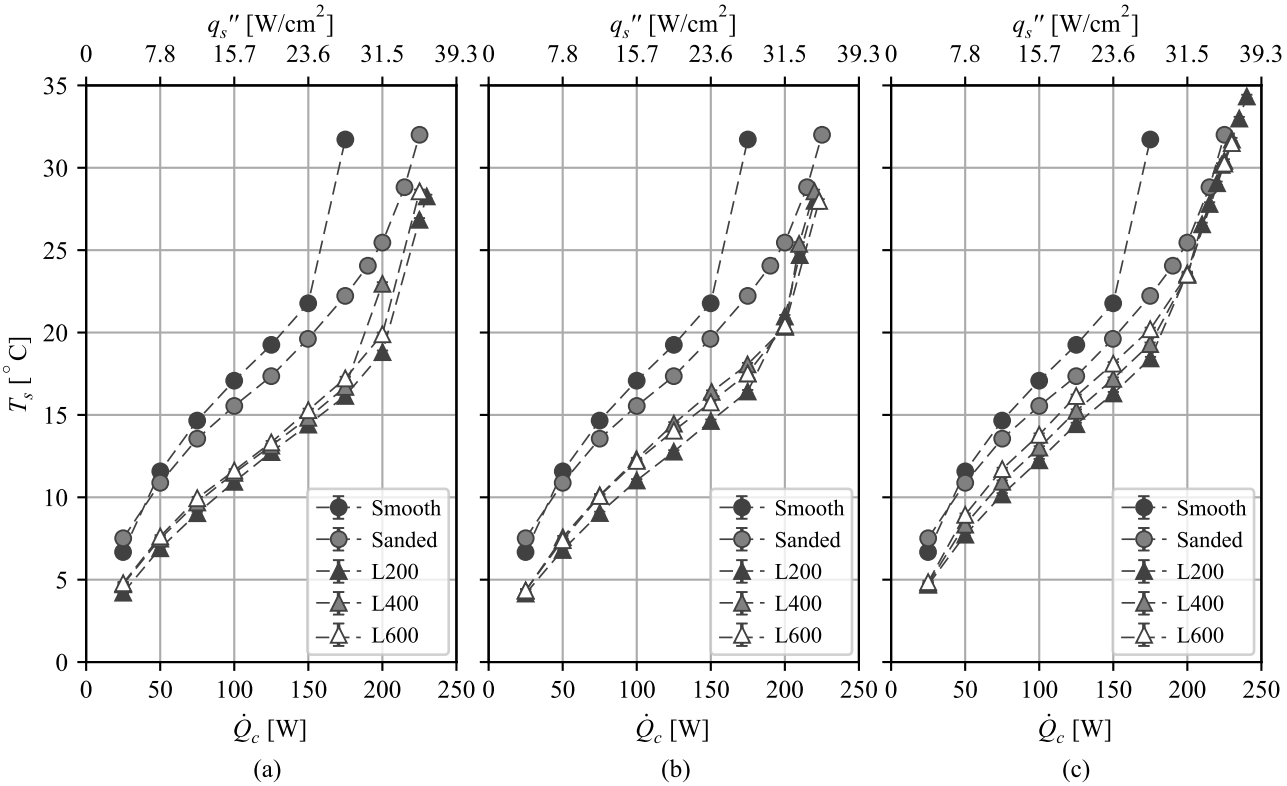

Figure 8: Surface temperature. Micro pillars spacing (a) S200, (b) S400, (c) S600.

The cooling unit outlet vapor mass quality is presented in Figure 9. Although all curves exhibit the same trend and values within the measuring uncertainty for the same heat load, it is noticeable the larger vapor mass quality for the modified surfaces. While the polished surface is the only surface with a vapor mass quality below 0.9 at the CHF point, others present values close to 0.95. This indicates the modified surfaces use the available liquid more efficiently, which allows larger CHF values.

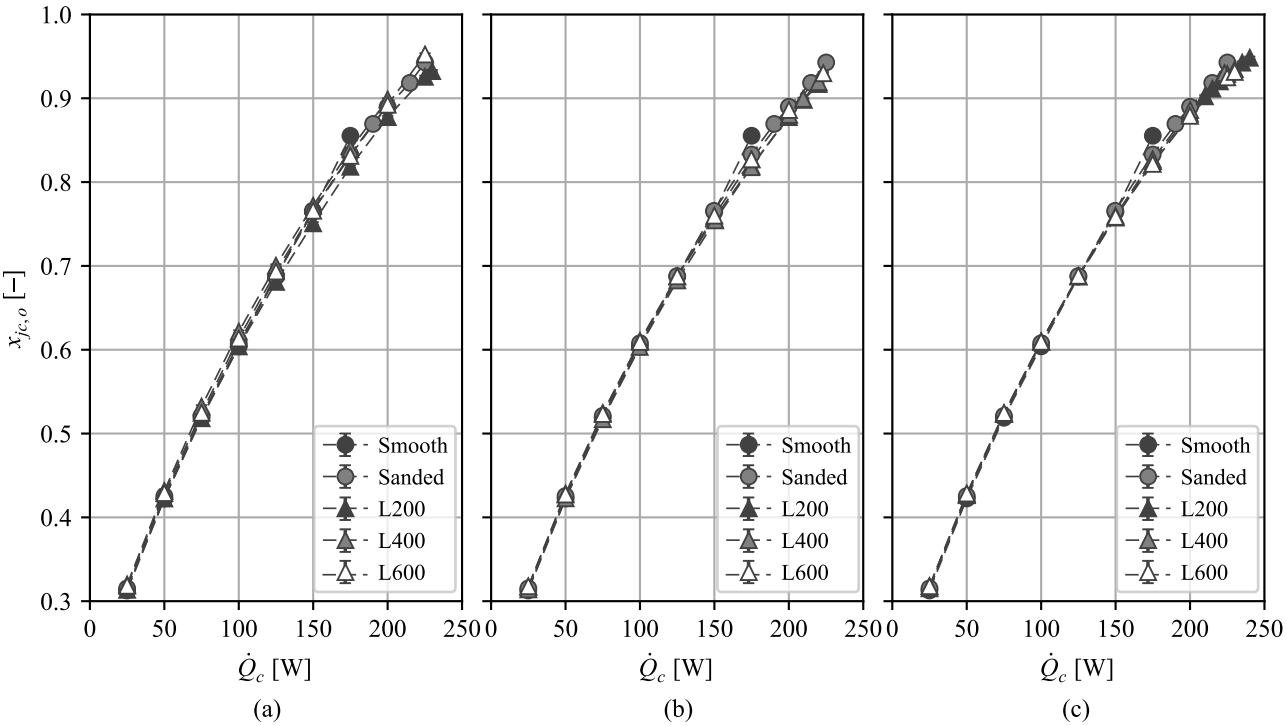

Figure 9: Vapor mass quality at the cooling cooling outlet. Micro pillars spacing (a) S200, (b) S400, (c) S600.

The so called boiling curves are presented in Figure 10. These curves differ from the traditional boiling curves since the later is built with a constant refrigerant mass flow rate. Differently, the refrigerant mass flow rate increases with the applied heat load for the presented results, as presented in Figure 4. Thus, the onset of CHF results from the interplay between the increasing liquid mass flux on the heated surface and the increasing rate of phase change due to boiling and evaporation of the liquid film (Carneiro *et al.*, 2018). Micro pillar surface present a great heat transfer enhancement with boiling curves far shifted to the left and a steep inclination when compared to smooth and sanded surfaces.

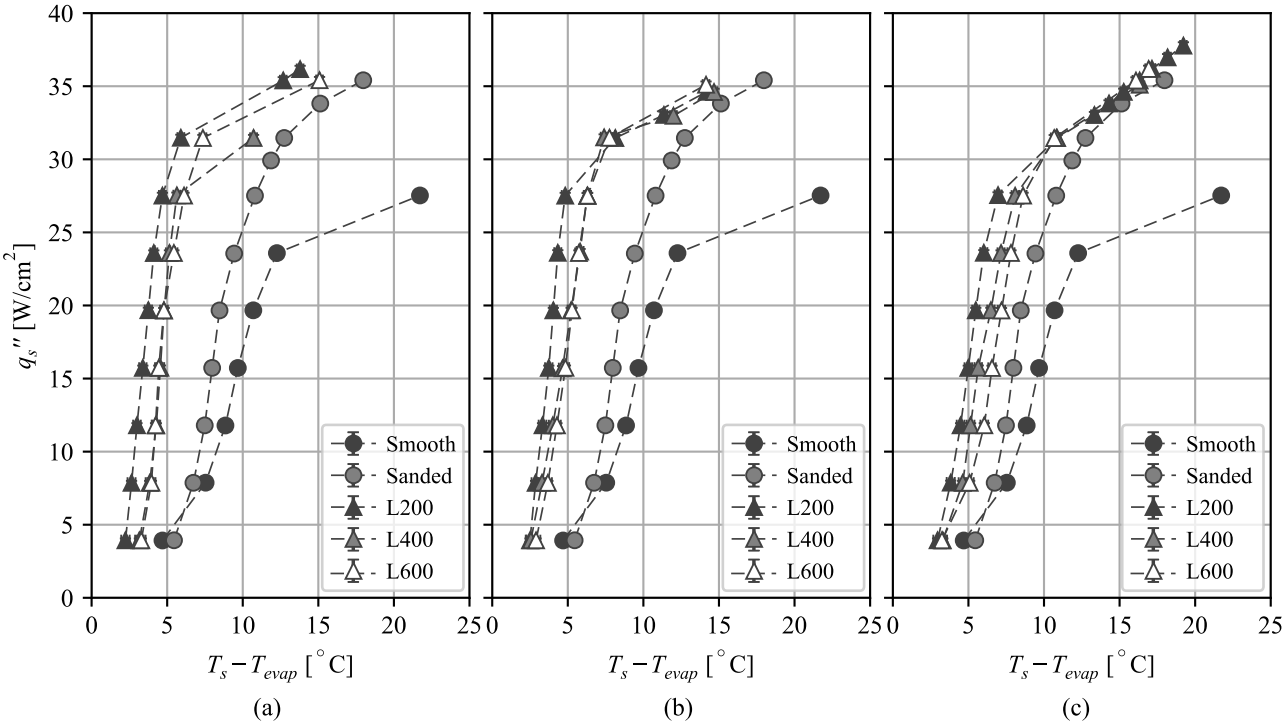

Figure 10: Adapted boiling curve. Micro pillars spacing (a) S200, (b) S400, (c) S600.

Although the surface modification presented a significant heat transfer enhancement, no significant CHF improvement has been statistically relevant for the surfaces evaluated. Additionally, the boiling curves represent how the experimental results are carried out in the heat up mode, this may indicate that a special effort must be consider in order to better characterize the CHF point. The heat transfer coefficient is the reciprocal result of the boiling curve and is presented in Figure 11.

As expected from the previous results, modified heat transfer surfaces provide significantly larger heat transfer coefficient for all the range of applied heat load. The heat transfer coefficient increases with the heat load for all surfaces and reaches its maximum value at heat loads around 175 W for the modified surfaces and 150 for the smooth one. The heat transfer coefficient increase for the ablated surfaces represents 1.6 to 3 times the value of the sanded surface. These values are for the S600 L600 and S200 L200 surfaces, respectively.

High-speed video sequence acquired for these surfaces indicate that the micro pillars are capable of maintaining the liquid film uniformly distributed over the heated surface. This results in more intensive boiling, which is observed due to the bubble disturbances in the surface grooves. Therefore, for heat loads up to 175 W, the great heat transfer coefficient improvements might be explained by a larger contribution of nucleate boiling on the heat transfer for the ablated surfaces. This is so, that varying the micro pillar spacing presents a great effect on the heat transfer coefficient. Larger micro pillar spacing may reduce the capillary effect and the liquid film uniformity over the surface. For example, the greater capillary effect expected for the S200 surfaces stands out and results in a larger liquid supply. This provides a larger boiling area, a larger number of nucleation sites and, consequently, larger heat transfer coefficient.

For heat loads larger than 175 W, the heat transfer coefficient of the micro pillars decreases significantly and approaches the values for the sanded surface. The high-speed video sequence also indicates that for these heat load values, the liquid film is restricted at the inner area of the heated surface. In other words, as the liquid film front within the surface groves flow to the outer part of the surface, it balances with the large liquid boiling rate. Therefore, the surface dry out starts at the outer part, reduces the boiling and convection area and, consequently, the heat transfer coefficient. As the amount of liquid over the heated surface reduces significantly, the cooling system is not able to sustain larger increase in the applied heat load. This triggers the surface temperature runaway reaching the critical heat flux.

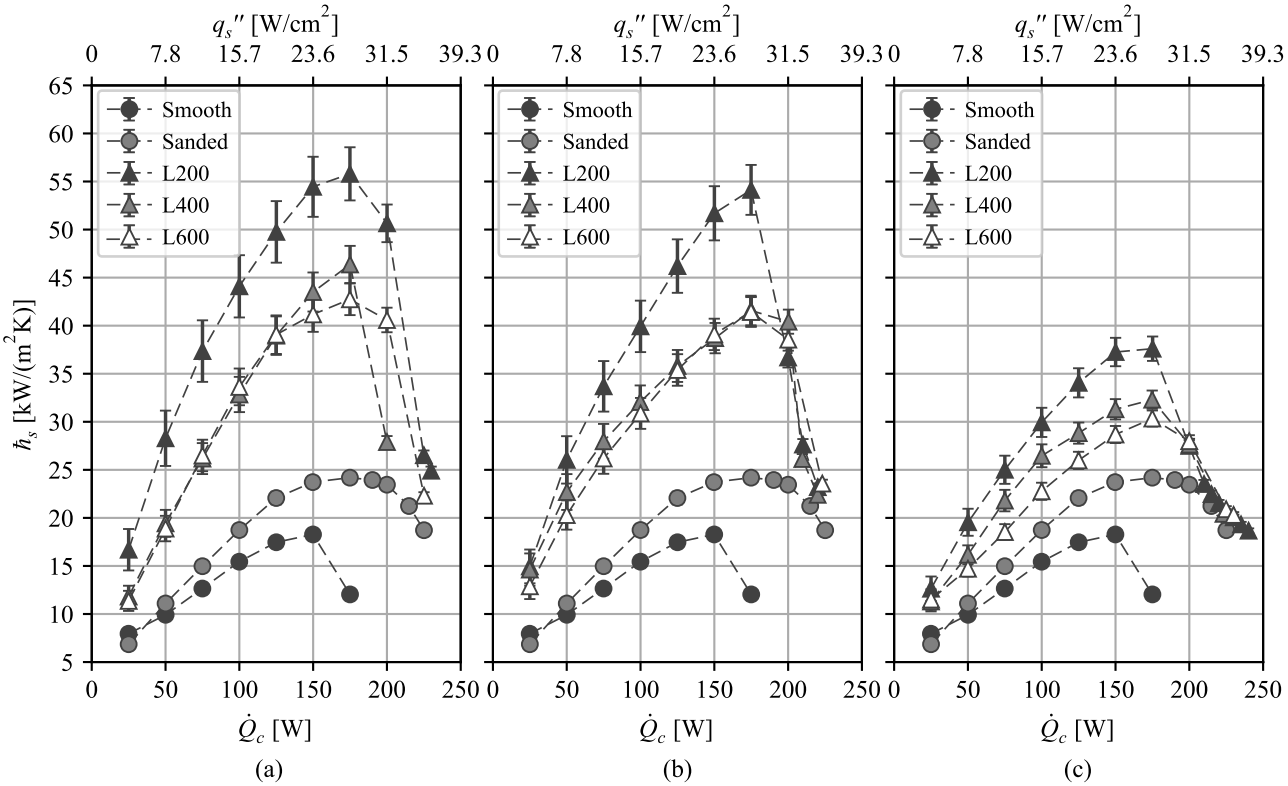

Figure 11: Heat transfer coefficient. Micro pillars spacing (a) S200, (b) S400, (c) S600.

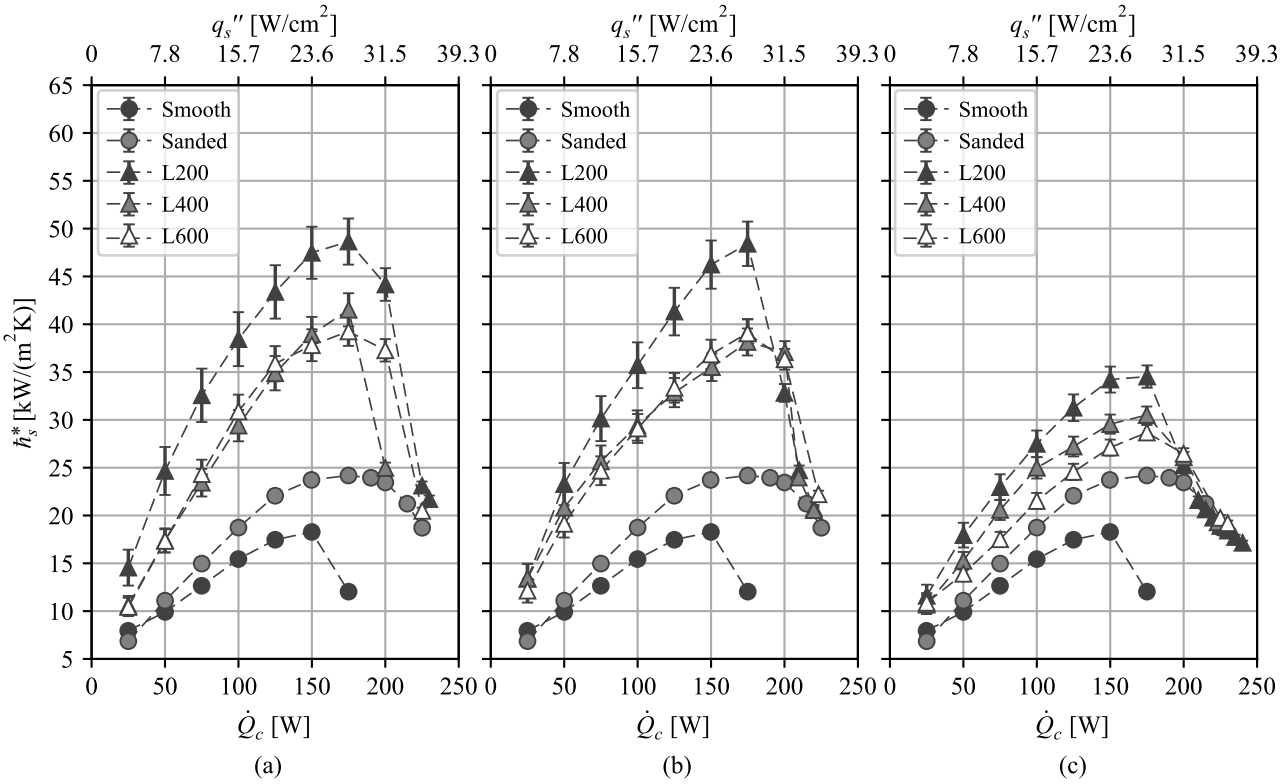

Figure 12: Heat transfer coefficient modified for the enhanced surface. Micro pillars spacing (a) S200, (b) S400, (c) S600.

Owing to the great number of influential heat transfer parameters, one that could be disregarded is the extension of the heat transfer surface area. This is accomplished by considering the total heat transfer surface area of the ablated surfaces. The unit cell surface area can be used to calculate a corrected heat transfer coefficient, Figure 12. The results point that, although the heat transfer coefficient decreases, the surface modification still presents a significant heat transfer performance enhancement for the S200 and S400 surfaces. This enhancement is much more modest for larger spacing,

S600 surfaces. On the other hand, if the surfaces with the same micro pillar spacing are considered, the effect on the heat transfer coefficient due to the micro pillar size is also diminished. That indicates the capillarity plays a significant role in the heat transfer performance, which is relatively similar for surfaces with the same micro pillar spacing.

4. Conclusions

The compact, oil free refrigeration system intended for high heat flux removal presented in previous works (Carneiro *et al.*, 2018, 2020; Oliveira and Barbosa Jr., 2017a,b) was investigated with resilient micro structured surfaces manufactured by laser ablation. The extended heat transfer surface area was measured and considered in the heat transfer performance analysis to help classify the surfaces features contributing to heat transfer enhancement. The heat transfer coefficient enhancement ranged from 1.6 to 3 times the baseline surface, which is a flat surface with a 400 sandpaper finishing. This wide range enhancement greatly depends on the micro pillars size and spacing. On the other hand, the refrigeration system parameters were not significantly affected by the surface modification. Further investigation regarding the effect of different laser ablation parameters and surface topography on the heat transfer performance is needed as an effort to shed more light on the key surface features that can enhance critical heat flux and heat transfer coefficient.

5. ACKNOWLEDGEMENTS

Financial support from the National Institute of Science Technology in Cooling and Thermophysics (CNPq (Grant No. 404023/2019-3, FAPESC Grant No. 2019TR0846), EMBRAPII and NIDEC GA (formerly Embraco) is gratefully acknowledged.

6. REFERENCES

Bell, I.H., Wronski, J., Quoilin, S. and Lemort, V., 2014. "Pure and pseudo-pure fluid thermophysical property evaluation and the open-source thermophysical property library coolprop". *Industrial & Engineering Chemistry Research*, Vol. 53, No. 6, pp. 2498–2508. doi:10.1021/ie4033999. URL http://pubs.acs.org/doi/abs/10.1021/ie4033999.

Carneiro, M.V.P., de Oliveira, P.A. and Barbosa Jr., J.R., 2018. "A compact refrigeration system based on multijet sprays for electronics thermal management". *Experimental Thermal and Fluid Science*, Vol. 97, pp. 180 – 191. ISSN 0894-1777. doi:https://doi.org/10.1016/j.expthermflusci.2018.03.005. URL http://www.sciencedirect.com/science/article/pii/S0894177718303339.

Carneiro, M.V.P. and Barbosa Jr., J.R., 2021. "A comparison of parallel and colliding jet arrays in a compact vapour compression heat sink for electronics cooling". *Applied Thermal Engineering*, Vol. 195, p. 117217. ISSN 1359-4311. doi:https://doi.org/10.1016/j.applthermaleng.2021.117217. URL https://www.sciencedirect.com/science/article/pii/S1359431121006554.

Carneiro, M., Provensi, A., Cavicchioli, P., Pereira, M. and Barbosa Jr., J., 2020. "A compact reverse rankine cycle combines surface enhancement and jet impingement to remove high heat fluxes". In *IIR Rankine Conference 2020*. Glasgow, Scotland, Vol. 2020-July, pp. 531–538. doi:10.18462/iir.rankine.2020.1214.

Khandekar, S., Sahu, G., Muralidhar, K., Gatapova, E.Y., Kabov, O.A., Hu, R., Luo, X. and Zhao, L., 2021. "Cooling of high-power leds by liquid sprays: Challenges and prospects". *Applied Thermal Engineering*, Vol. 184, p. 115640. ISSN 1359-4311. doi:https://doi.org/10.1016/j.applthermaleng.2020.115640. URL https://www.sciencedirect.com/science/article/pii/S1359431120331227.

Kubiak, K., Wilson, M., Mathia, T. and Carval, P., 2011. "Wettability versus roughness of engineering surfaces". *Wear*, Vol. 271, No. 3, pp. 523 – 528. ISSN 0043-1648. doi:https://doi.org/10.1016/j.wear.2010.03.029. URL http://www.sciencedirect.com/science/article/pii/S0043164810001390. The 12th International Conference on Metrology and Properties of Engineering Surfaces.

Li, B., Kuo, H., Wang, X., Chen, Y., Wang, Y., Gerada, D., Worall, S., Stone, I. and Yan, Y., 2020. "Thermal management of electrified propulsion system for low-carbon vehicles". *Automotive Innovation*, Vol. 3, pp. 2522–8765. doi:10.1007/s42154-020-00124-y.

Lijun, L., Zhang, Q., Zhai, Z.J., Yue, C. and Ma, X., 2020. "State-of-the-art on thermal energy storage technologies in data center". *Energy and Buildings*, Vol. 226, p. 110345. ISSN 0378-7788. doi:https://doi.org/10.1016/j.enbuild.2020.110345. URL https://www.sciencedirect.com/science/article/pii/S0378778819336771.

Martendal, C., Silveira, C., Pereira, M. and Fredel, M., 2020. "Wettability modification of laser textured copper surfaces applied to phase change heat transfer". *Journal of Laser Applications*, Vol. 32, No. 3. doi:10.2351/7.0000094.

Oliveira, P.A. and Barbosa Jr., J.R., 2017a. "Novel two-phase jet impingement heat sink for active cooling of electronic devices". *Applied Thermal Engineering*, Vol. 112, pp. 952 – 964. ISSN 1359-4311. doi:https://doi.org/10.1016/j.applthermaleng.2016.10.133. URL

http://www.sciencedirect.com/science/article/pii/S1359431116326436.

Oliveira, P.A. and Barbosa Jr., J.R., 2017b. "Performance Assessment of Single and Multiple Jet Impingement Configurations in a Refrigeration-Based Compact Heat Sink for Electronics Cooling". *Journal of Electronic Packaging*, Vol. 139, No. 3. ISSN 1043-7398. doi:10.1115/1.4036817. URL https://doi.org/10.1115/1.4036817. 031005.

Parizad Benam, B., Sadaghiani, A.K., Yağcı, V., Parlak, M., Sefiane, K. and Koşar, A., 2021. "Review on high heat flux flow boiling of refrigerants and water for electronics cooling". *International Journal of Heat and Mass Transfer*, Vol. 180, p. 121787. ISSN 0017-9310. doi:https://doi.org/10.1016/j.ijheatmasstransfer.2021.121787. URL https://www.sciencedirect.com/science/article/pii/S0017931021008929.

Rong, A., Pang, L., Jiang, X., Qi, B. and Shi, Y., 2021. "Analysis and comparison of potential power and thermal management systems for high-speed aircraft with an optimization method". *Energy and Built Environment*, Vol. 2, No. 1, pp. 13–20. ISSN 2666-1233. doi:https://doi.org/10.1016/j.enbenv.2020.06.006. URL https://www.sciencedirect.com/science/article/pii/S2666123320300623.

Shurong, L., Shi, Y. and Chen, G., 2020. "A lithium-ion battery-thermal-management design based on phase-change-material thermal storage and spray cooling". *Applied Thermal Engineering*, Vol. 168, p. 114792. ISSN 1359-4311. doi:https://doi.org/10.1016/j.applthermaleng.2019.114792. URL https://www.sciencedirect.com/science/article/pii/S1359431119355486.

Silk, E.A., Kim, J. and Kiger, K., 2006. "Spray cooling of enhanced surfaces: Impact of structured surface geometry and spray axis inclination". *International Journal of Heat and Mass Transfer*, Vol. 49, No. 25, pp. 4910–4920. ISSN 0017-9310. doi:https://doi.org/10.1016/j.ijheatmasstransfer.2006.05.031. URL https://www.sciencedirect.com/science/article/pii/S0017931006003498.

Wiedenheft, K.F., Guo, H.A., Qu, X., Boreyko, J.B., Liu, F., Zhang, K., Eid, F., Choudhury, A., Li, Z. and Chen, C.H., 2017. "Hotspot cooling with jumping-drop vapor chambers". *Applied Physics Letters*, Vol. 110, No. 14, p. 141601. doi:10.1063/1.4979477. URL https://doi.org/10.1063/1.4979477.

Xu, R., Wang, G. and Jiang, P., 2021. "Spray Cooling on Enhanced Surfaces: A Review of the Progress and Mechanisms". *Journal of Electronic Packaging*, Vol. 144, No. 1. ISSN 1043-7398. doi:10.1115/1.4050046. URL https://doi.org/10.1115/1.4050046. 010802.

Yang, J., Chow, L.C. and Pais, M.R., 1996. "Nucleate Boiling Heat Transfer in Spray Cooling". *Journal of Heat Transfer*, Vol. 118, No. 3, pp. 668–671.

7. RESPONSIBILITY NOTICE

The authors are solely responsible for the printed material included in this paper.